International Journal of Industrial Chemistry (2019) 10:175–191
https://doi.org/10.1007/s40090-019-0182-7

RESEARCH

# Application of (polyaniline/zeolite X) composite as anticorrosion coating for energy recovery devices in RO desalination water plants

**Ahmed H. Abdel Aziz[1] · Tarek S. Jamil[2] · Marwa S. Shalaby[3] · Ahmed M. Shaban[2] · Eglal R. Souaya[1] · Nabil A. Abdel Ghany[4]**

Received: 5 April 2018 / Accepted: 14 March 2019 / Published online: 22 March 2019


**Abstract**
Reverse osmosis desalination water plants have several operational issues such as corrosion in many areas like energy recovery devices that are accustomed to restore energy and scale back prices. Thus, there is a necessity to reduce the corrosion rate of the devices utilized in energy recovery. This study focuses on protection of some metals and alloys that are utilized in this industry by introducing a new anticorrosion coating. The new anticorrosion coating was formulated by the interaction of polyaniline and X-type zeolite that is employed as hosting material. Polyaniline was first formulated by conventional oxidation polymerization method of aniline in acidic medium at temperature below 5 °C by using ice bath. Then, ammonium persulphate was used as oxidizer. Numerous characterization techniques were used to demonstrate the encapsulation of polyaniline in X-type zeolite frames such as IR, UV–visible spectroscopy, scanning electron microscopy, transmission electron microscope, energy-dispersive X-ray and X-ray diffraction. The new anticorrosion coating was evaluated by using weight loss technique, Tafel polarization and electrochemical impedance spectroscopy; all of these techniques showed the effective anticorrosion properties of the prepared coating in which the corrosion rate from the polarization curves results, for all coated samples, was less than the bare ones as it recorded 2.403, 1.094, 23.48, 35.09 MPY for bare 304 and 316 stainless steel, Al and carbon steel, respectively, and 0.3132, 0.2733, 0.2506, 10.81 MPY for the coated samples. Corrosion results showed a noteworthy protection of the tested metals and alloys in saline water coated with the polyaniline/zeolite X.

**Keywords** Polymer composites · Coatings · Corrosion · Energy recovery

**Abbreviations**

| | |
|---|---|
| $2\theta$ | 2 theta |
| CR | Corrosion rate |
| DTG | Differential thermogravimetric analysis |
| MPY | Millie inch per year |
| PANI | Polyaniline |
| EIS | Electrochemical impedance spectroscopy |
| RO | Reverse osmosis process |
| SEM | Scanning electron microscope |
| TDS | Total dissolved solids |
| TEM | Transmittance electron microscope |
| TGA | Thermogravimetric analysis |
| XRD | X-ray diffraction analysis |

✉ Ahmed H. Abdel Aziz
ahmedhelmyabdelaziz@yahoo.com

[1] Chemistry Department, Faculty of Science, Ain Shams University, Khalifa El-Maamon St., Abbasiya sq., Cairo 11566, Egypt

[2] Water Pollution Control Department, National Research Center, 33 El Buhouth St., Dokki, Cairo 12311, Egypt

[3] Chemical Engineering and Pilot Plant Department, National Research Centre, 33 El Buhouth St., Dokki, Cairo 12311, Egypt

[4] Electrochemistry and Corrosion Lab., Physical Chemistry Department, National Research Centre, 33 El Buhouth St., Dokki, Cairo 12311, Egypt

## Introduction

Currently, one of the most important issues in several regions of the globe is water inadequacy. This inadequacy is caused by several factors, such as global warming, maximized urbanization, explosive population growth, excessive usage and altered water resource usage patterns. Water shortage is the issue limiting economic and social development in various cases. Water purification is required wherever water is saline; as much as 98% of the water in the world is saline (seawater, saline groundwater

and saline seas) and therefore not appropriate for use as a beverage or in agriculture [1].

Desalination processes separate saline feed water, which may be brackish water or seawater, into product water with low salinity and concentrated brine. Such separation methods require energy input to manage many parameters, such as those of the separation method itself and the salinity and temperature of the incoming saline water [2]. The minimization of this needed energy is crucial because such minimization increases the value of the product water and reduces the generation of greenhouse gases and therefore reduces the disposal of various pollution products into the ocean or atmosphere. Therefore, a mechanism to decrease energy consumption is necessary; for this reason, energy recovery devices are used. The main function of an energy recovery device is to recover much of the energy held in the pressurized RO concentrate stream. Before continuing to disposal or treatment, the concentrate is sent through an energy recovery device, and the recovered energy is used to partially power the pumps [3].

In groundwater, the concentrations of many ions can vary within wide limits, and such variation can have a marked impact on the pitting and crevice corrosion of stainless steel (SS). Such materials tend to undergo pitting corrosion or other local corrosion in media containing aggressive ions, such as chloride [4]. Modern surface modification technology is becoming increasingly necessary in the enhancement of the corrosion resistance of many materials. If aluminiferous materials are not custom made, corrosion can propagate very rapidly [4].

Conducting polymers have become one of the most attractive subjects of investigation in recent decades. Their unique properties, such as electrical conductivity, reversible electrochemical behaviour and the possibility of both chemical and electrochemical synthesis, make them useful in a wide range of applications [4].

These materials are utilized in various technical applications, including chemical and electrochemical sensors [5], corrosion protection [6] and the removal of toxic materials [7]. The most popular conducting polymer is polyaniline (PANI) due to its acceptable chemical stability, comparatively high levels of electrical conductivity and monomer availability and ease of polymer synthesis. Several studies have targeted the corrosion protection performance of conducting polymers [8], particularly PANI [9]. PANI is often polymerized directly on a metal substrate acting as a protective primer film [10] or can alternatively be used as an additive in blends with insulating polymers [11]. Such blends are preferred (especially if a low concentration of PANI is adequate for active functionality) since the desired mechanical properties of coatings are often provided by the proper choice of the host polymer matrix.

Polymers can also be encapsulated for many reasons; however, the primary reasons are to shield materials from atmospheric and alternative types of chemical attack and for the separation of polymer chains to reduce inter-chain effects and improve the mechanical, thermal and chemical stability [12].

Zeolites are a category of micro-porous crystalline alumina silicates based on a 3D network of oxygen ions. Zeolites are made from $AlO_4$ and $SiO_4$ tetrahedra linked to each other by shared oxygen ions [13]. The encapsulation of PANI in zeolite channels may be a promising strategy to insert polymer chains into the nanometre-sized zeolite channels to obtain nanocomposite materials with novel unique properties. A nanocomposite of PANI with zeolite prepared by encapsulation will exhibit electronic, mechanical, chemical and optical properties higher than those of pure conducting PANI [14].

This work introduces a new anticorrosion coating that depends on the encapsulation of PANI chains within zeolite X channels. The prepared P/Z composite was characterized by infrared (IR) and UV–visible spectroscopy, scanning electron microscopy (SEM), transmission electron microscopy (TEM), thermogravimetric analysis (TGA), energy-dispersive X-ray (EDX) spectroscopy and X-ray diffraction (XRD) and was applied as a coating on the surface of various materials including SS (304 and 316 grade), aluminium and carbon steel. The anticorrosion properties were studied by weight loss, potentiodynamic techniques and electrochemical impedance spectroscopy.

## Experimental

### Materials and methods

Aniline was obtained from Alpha Chemika, India, ammonium persulphate was obtained from Oxford Laboratory, India, and formic acid was obtained from El-Goumhouria Co., Cairo, Egypt; these materials were used without further purification. Sodium hydroxide and HCl were purchased from Fluka Chemical Co. Zeolite X was obtained from the National Research Centre (NRC), Egypt. Carbon steel, 304 and 316 stainless steel (SS304 and SS316, respectively) and aluminium were obtained from a local market, Egypt (Table 1 shown there composition) and used for corrosion studies. Prior to all measurements, samples were abraded with a series of emery paper from 180 to 1200 grade. The specimens were thoroughly washed with bi-distilled water, dried and degreased with acetone. The test solution was saline water with a TDS of 100,000 ppm.

**Table 1** Chemical composition of carbon steel, SS304 and SS 316

| Composition (wt%) | Material | | |
|---|---|---|---|
| | C-steel | SS304 | SS316 |
| Cr | – | 18.18 | 18.00 |
| Ni | – | 8.48 | 10.00 |
| Mn | – | 1.75 | 2.00 |
| Si | – | 0.57 | 0.75 |
| Mo | – | – | 1.66 |
| C | 0.17 | 0.051 | 0.08 |
| N | 0.007 | 0.05 | 0.10 |
| S | 0.05 | 0.005 | 0.03 |
| P | 0.05 | 0.028 | 0.045 |
| Fe | – | Reminder | Reminder |

## Synthesis of polyaniline/zeolite X composite

The P/Z composite was synthesized via oxidative polymerization in which 5.0 mL aniline was vigorously stirred in 250 mL of HCl (1 M) and then cooled to below 5 °C (by using an ice bath). Zeolite X with a concentration of 1% (w/w) with respect to aniline monomer was added to the solution. A total of 250 mL of a pre-cooled 0.3 M $(NH_4)_2S_2O_8$ ammonium persulphate solution was slowly added under vigorous stirring to the monomer solution over a period of 30 min. The reaction mixture was stirred for approximately 2 h at low temperature (0–5 °C) and left unstirred overnight at room temperature. When the reaction was completed, the dark green precipitate resulting from the polymerization reaction was filtered and washed with distilled water and then with dilute HCl solution until the washing liquid was colourless. To remove oligomers and other non-polymeric impurities, the precipitate was washed thoroughly with methanol and distilled water. The polymer was dried at 50–60 °C in an oven, powdered in a mortar and stored for processing.

To make PANI soluble in formic acid for coating and composite formation, the resulting polymer composite was treated with 0.5 M NaOH solution for 2 h and then washed with distilled water and dried in an oven at 60 °C. A total of 0.5 g of base-treated PANI, emeraldine base (EB), was dissolved in 50 mL of formic acid. The polymer solution was filtered to remove any non-dissolvable solids.

For preparation of the coating solution, 5 g of nylon 6 was mixed with 50 mL of polymer composite (EB) in formic acid (1% w/v) in a beaker (100 $cm^3$), stirred for two hours at room temperature and left for another 2 h without stirring. The excess solvent was evaporated by heating the coating solution at ~ 60 °C in an oven, leaving the substrate coated with a solid thin film.

## Characterization studies

### FTIR analysis

The FTIR spectra of PANI/zeolite X composite were taken with KBr discs using FTIR spectrophotometer (460 plus) in the range of 4000–400 $cm^{-1}$ in Micro analytical centre at Cairo University, Egypt.

### UV spectra analysis

The UV–Vis spectra of the PANI/zeolite X composite in the wavelength range of 200–800 nm were recorded with UV-3101PC Shimadzu in Micro analytical centre at Cairo University.

## Scanning electron microscope (SEM) analysis

The scanning electron micrograph of polyaniline, zeolite X and PANI/zeolite X composite was analysed using Model Quanta 250 FEG (Field Emission Gun) with accelerating voltage 30 kV, FEI Company, Netherlands, in the Egyptian Mineral Resources Authority, Central Laboratories Sector.

### X-ray diffraction (XRD) analysis

The powder X-ray diffraction (XDR) of polyaniline, zeolite X and PANI/zeolite X composite was analysed using Bruker D8 advance instrument with CuKα1 target with secondary monochromator 40 kV, 40 mA, in National Research Centre, Dokki, Giza, Egypt.

### Transmitting electron microscope (TEM) analysis

The transmitting electron micrograph of polyaniline, zeolite X and PANI/zeolite X composite was analysed using the JEOL JEM-2100 LaB6 transmission electron microscope (TEM) at National Research Centre, Egypt. The JEOL JEM-2100 LaB6 transmission electron microscope (TEM) is equipped with the high-resolution (HRP) style objective-lens pole piece to achieve point resolution as small as 0.23 nm—small enough to observe lattice structure in many crystalline materials. The instrument operates at a high tension of up to 200 kV, corresponding to an electron wavelength of 2.5 pm. Image acquisition is performed with a Gatan Orius bottom-mount, 14-bit, 11-megapixel CCD camera.

### Thermal (TGA) analysis

Thermogravimetric (TGA) and differential (DTG) thermogravimetric analyses were carried out under $N_2$-atmosphere (30 mL/min) using detectors model TGA-50H Shimadzu thermal analyser. The rate of heating of the sample was kept

at 10 °C/min in Micro analytical centre at Cairo University, Egypt.

#### Energy-dispersive X-ray (EDX) analysis

The energy-dispersive X-ray analysis of PANI/zeolite X composite and stainless steel (bare and coated) were analysed using EDX unit (energy-dispersive X-ray analyses), with accelerating voltage 30 kV, magnification 14 × up to 1,000,000 and resolution for Gun) FEI Company, Netherlands, in the Egyptian Mineral Resources Authority, Central Laboratories Sector.

### Corrosion studies

#### Weight loss measurements

Gravimetric corrosion measurements were carried out; both bare and coated prepared samples were cut into "1 × 1 × 3 cm" coupons and immersed in 100 mL of saline water. The difference in the mass of coupons before and after immersion was determined by using an analytical balance with accuracy 0.001 mg, and the immersion time was 72 h at 25 °C. The investigations were carried out at open air without aeration.

The corrosion rate (CR) (Eq. 1) for bare and coated samples was calculated from the following equation:

$$\mathrm{CR} = \frac{\left(W_1 - W_2\right)}{AT} \tag{1}$$

where $W_1$ is the weight of the specimen before corrosion, $W_2$ is the weight of the specimen after corrosion, $A$ is the total area of the specimen, $T$ is the corrosion time, and CR is the corrosion rate.

Additionally, the inhibition efficiency (IE) (Eq. 2) of the prepared coating for the corrosion of these samples was obtained from the CR value by using the following equation:

$$\mathrm{IE}\,(\%) = \left(\frac{\mathrm{CR}-\mathrm{CR}^{\circ}}{\mathrm{CR}}\right) \times 100 \tag{2}$$

where CR and CR° are the corrosion rates of the bare and coated samples, respectively.

#### Potentiodynamic polarization studies

Electrochemical experiments were performed in a traditional three-electrode system consisting of working, auxiliary and reference electrodes. Working electrodes with a surface area of 2 $cm^2$ were used; the chemical compositions are given in Table 1. The electrodes were abraded with a series of emery paper from 180 to 1200 grade. Then, the samples were cleaned with acetone, washed with distilled water and quickly inserted into the cell. All experiments were carried out in 100 mL of test solution. A saturated calomel electrode (SCE) and platinum electrode were used as reference and auxiliary electrodes, respectively. A stirred electrolyte, saline water at 25 ± 3 °C, was used as a corrosive medium. The open-circuit potential of the metal immersed in the test solution was monitored using an electronic multimeter (Type E scord-EDM-2116). The electrode was allowed to stabilize in the electrolyte until the potential change was < 0.1 mV/min. This potential was taken as the steady-state potential.

Potentiodynamic polarization studies were carried out in the potential range ± 200 mV versus corrosion potential ($E_{corr}$) at a scan rate of 0.5 mV/s. The pitting susceptibility was characterized by means of cyclic anodic polarization curves. The current limit for reversing the potential scan was $10^{-3}$ A/$cm^2$. The studies were performed with a model 352/252 corrosion measurement system, which consists of an EG&G potentiostat/galvanostat, model 273 A. The scan direction was reversed at the anodic limit. In subsequent analysis of the digitally recorded data, the pitting potential ($E_{pitt}$) was defined at a sustained anodic current density, and the re-passivation potential was taken to be the point at which the reverse scan current crossed that of the forward scan. Tafel extrapolations were used to obtain the corrosion current density ($i_{corr}$) and thus calculate CR from the polarization scans.

#### Electrochemical impedance spectroscopy

Electrochemical investigations were carried out in a three-electrode conventional glass cell containing the test solution at 25 ± 3 °C using an Autolab PGSTAT 302N potentiostat/galvanostat. The potential of the working electrode was measured against an Ag/AgCl reference electrode ($E^{\circ}$ = 0.203 V versus SHE), while pure Pt foil was used as a counter electrode. The exposed surface area was 2 $cm^2$. Electrochemical impedance spectroscopy (EIS) of the electrodes was carried out with an input signal of 10 mV peak to peak in the frequency range from 100 kHz to 10 Hz with an alternating current of 0.1 mA. Nyquist and Bode plots were acquired by Nova 1.11.2 software from Autolab. Before each experiment, the working electrode was immersed in test solution until a steady state was reached; then, the impedance data were recorded and fitted to the theoretical data according to the proposed equivalent circle.

In the equivalent circuit (Fig. 6i), $R_s$ represents the solution resistance, $R_{ct}$ represents the charge transfer resistance, and CPE represents a constant phase element. An excellent fit was obtained with this model for all experimental data. The CPE represents the deviation from the true capacitance behaviour. To describe a frequency-independent phase shift between an applied alternating potential and its current response, CPE is used instead of capacitance ($C$).

CPE (Eq. 3) is defined by the following mathematical expression [15, 16]:

$$\mathrm{ZCPE} = \frac{1}{Y_0(jw)^n} \tag{3}$$

where $Z_{\mathrm{CPE}}$ represents the impedance of CPE, $Y_0$ is a proportional factor, $w$ is the angular frequency, $j = \sqrt{-1}$ is the imaginary number, and $n$ is the exponential term of CPE. $n$ has many different definitions and can be associated with a distribution of reaction rates [16] and a non-uniform current distribution [17, 18].

The angular frequency ($\omega$) is the angular frequency at which the imaginary impedance ($Z''$) is maximum and can be calculated as:

$$\omega = \left(\frac{1}{R_c Y_0}\right)^{1/n} \tag{4}$$

Therefore, $C$ (Eq. 5) of the double layer for both cases is calculated using the following equation:

$$C_{\mathrm{dl}} = \left(Y_0 R_{\mathrm{ct}}^{1-n}\right)^{\frac{1}{n}} \tag{5}$$

where $C_{\mathrm{dl}}$ is the double-layer capacitance, $Y_0$ is the magnitude of CPE, $R_{\mathrm{ct}}$ is the charge transfer resistance, and $n$ is the CPE exponent. Depending on $n$, CPE can represent resistance ($Y_0 = R$, $n = 0$), capacitance ($Y_0 = C$, $n = 1$), inductance ($Y_0 = L$, $n = -1$) or Warburg impedance ($n = 0.5$, $Y_0 = W$) [19].

IE (%) is calculated using the following equation (Eq. 6):

$$\mathrm{IE}\,(\%) = \left(\frac{R_{\mathrm{ct}} - R_{\mathrm{ct}}^0}{R_{\mathrm{ct}}^0}\right) \times 100 \tag{6}$$

where $R_{\mathrm{ct}}$ and $R_{\mathrm{ct}}^0$ are the charge transfer resistances for coated and bare steel, respectively.

## Results and discussion

### Characterization studies

The Fourier transform infrared (FTIR) spectra of zeolite X, PANI and the P/Z composite containing 1 wt% zeolite X are shown in Fig. 1. The absorption bands observed at 3436 $\mathrm{cm}^{-1}$ and 1690 $\mathrm{cm}^{-1}$ were attributed to the N–H stretching vibration mode and $NH_2$ deformation in the aniline unit, respectively, which are characteristic of PANI [20, 21]. The asymmetric vibration mode of C=C in the quinoid and benzenoid ring system in PANI was observed at 1586 and 1490 $\mathrm{cm}^{-1}$, respectively. The C-N stretching vibration mode of the quinoid ring of PANI was observed at 1303 $\mathrm{cm}^{-1}$, and the band at 1233 $\mathrm{cm}^{-1}$ corresponded to the benzenoid ring system. The C–H bending mode (in-plane vibration) was observed at 1147 $\mathrm{cm}^{-1}$, which is evidence for the polymerization of PANI. Out-of-plane C–H deformation

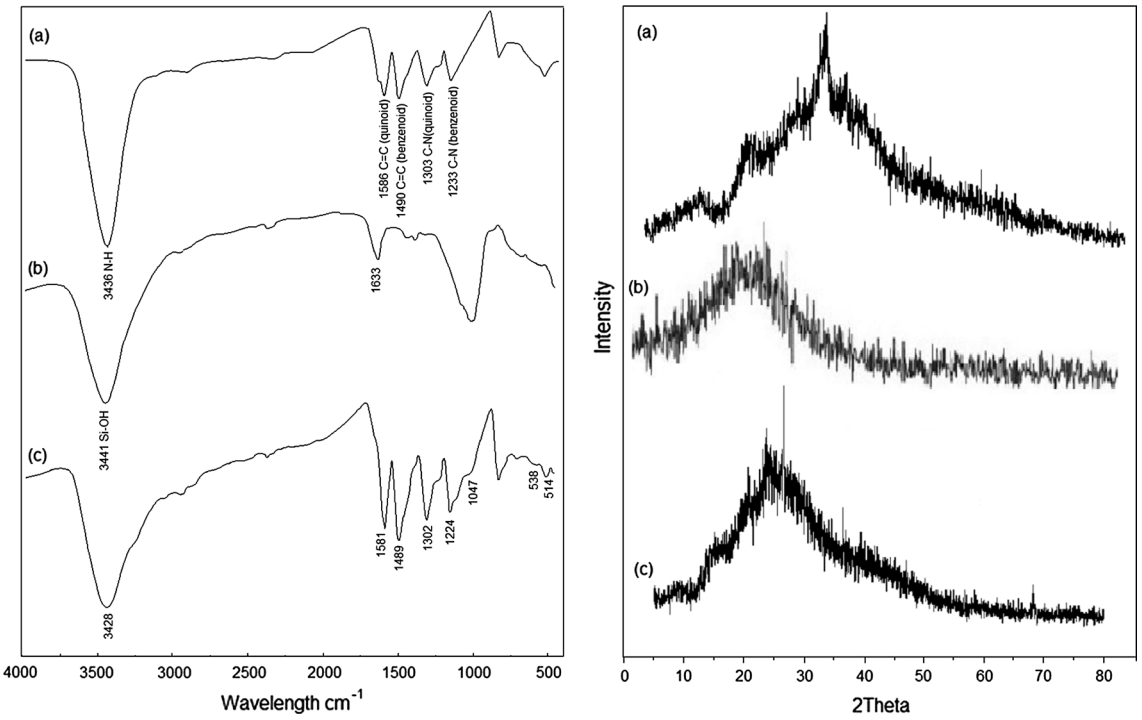


**Fig. 1** Infrared spectra and XRD pattern of **a** polyaniline, **b** zeolite X and **c** polyaniline/zeolite X composite

vibrations of the aromatic ring were observed at 822 and 712 $cm^{-1}$ [22]. These data agreed well with the results from other previous papers [23, 24]. For zeolite X, there was a noteworthy change from 3463 to 3441 $cm^{-1}$, which was attributed to silicon-hydroxyl groups, while the bands at 1080 $cm^{-1}$ and 1633 $cm^{-1}$ belonged to the absorption of hydroxyl water and hydroxyl, respectively, by Si–OH [25]. Characteristic bands of zeolites have previously been found [26] at 860–1230 $cm^{-1}$ and 420–500 $cm^{-1}$; here, bands were found at 1194 and 465 $cm^{-1}$, as shown in Fig. 1b. The first band at 1194 $cm^{-1}$ was assigned to an asymmetric stretching mode, and the other band was assigned to a bending mode of the T–O bond, where T refers to Si and Al. The crystal structure of zeolite may depend on these bands or others.

In the spectrum of the P/Z composite (Fig. 1c), the 3436 $cm^{-1}$ band shifted to 3428 $cm^{-1}$ due to the stretching frequency of the N–H group in PANI [27]. This spectrum also showed bands at 1581 $cm^{-1}$ and 1489 $cm^{-1}$, which were attributed to the quinine and benzene rings observed at 1586 $cm^{-1}$ and 1490 $cm^{-1}$ in PANI. New absorption peaks at 1047, 538 and 514 $cm^{-1}$ could be assigned to the presence of zeolite in the prepared composite [28]. Therefore, the FTIR spectra of the P/Z composite exhibit bands characteristic of both PANI and zeolite X, which confirmed the presence of both components in the P/Z composite.

The UV–Vis absorption spectra for PANI and the P/Z composite in DMSO solvent are shown in Fig. 2. The spectrum of the composite showed a characteristic peak at 339 nm and a broad peak at 623 nm. The first peak corresponds to the $\pi$–$\pi^*$ transition and agrees well with the standard band for PANI EB at ~ 330–340 nm [28]. The second peak at 623 nm may be assigned to the exciton transition (which results from the process of charge transfer between the benzenoid ring through the highest occupied energy level and the quinonoid ring through the lowest unoccupied energy level), which is quite weak in these polymers [29]. The oxidation state of PANI was measured from this exciton band, which has been determined at ~ 637 nm for "standard"

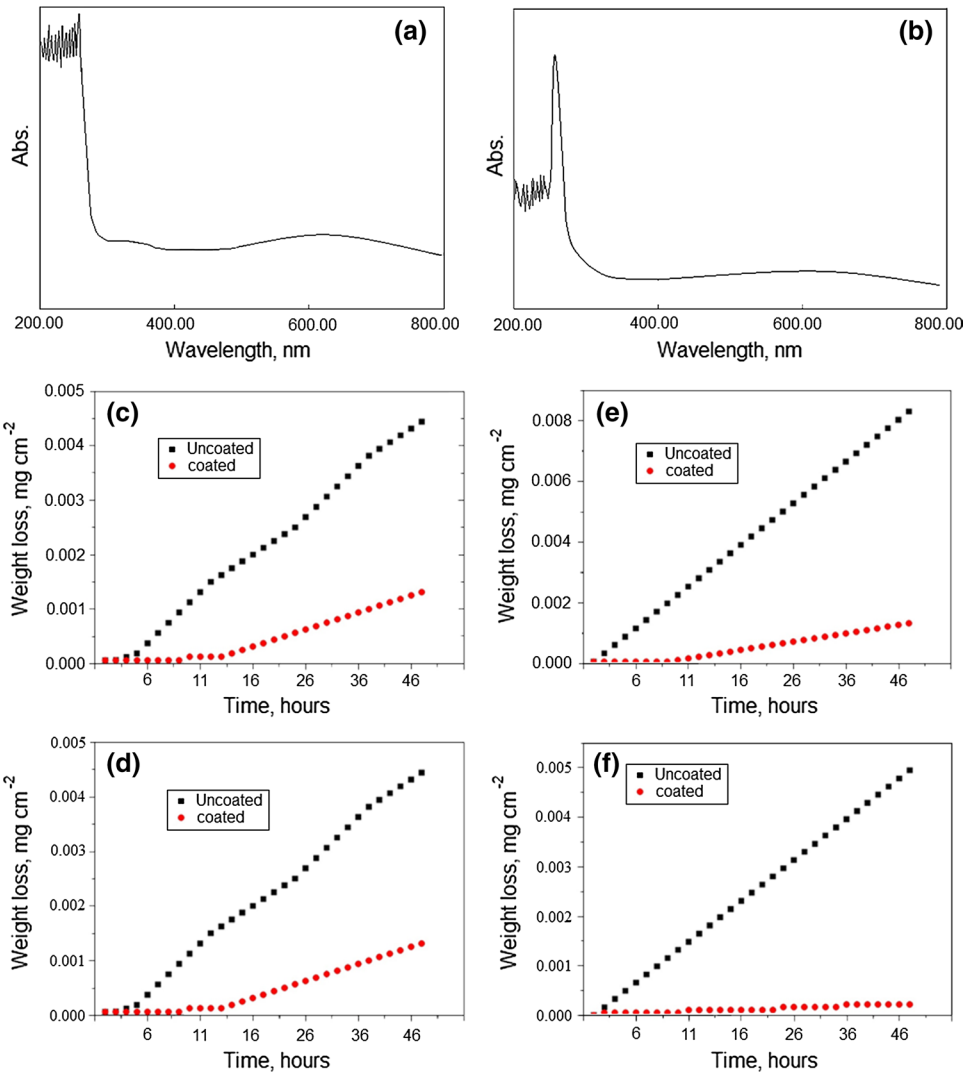


**Fig. 2** UV–visible spectra of **a** polyaniline and **b** polyaniline/zeolite X composite and the measurement of weight loss of bare (with black colour) and coated (with red colour) for **c** SS304, **d** SS316, **e** Al and **f** C-steel in saline water

EB [28]. The UV–Vis absorption spectra of the P/Z composite revealed a blue shift from the peak location for pure PANI, reflecting a diminished conjugated chain length of PANI in the P/Z composite [28, 30].

The XRD patterns were recorded for PANI, zeolite X and P/Z composite as shown in Fig. 1. The intensity of the XRD pattern peaks may be influenced by crystallinity or by PANI chain order within the composite structure. In the XRD patterns of zeolite X, peaks were recorded at $2\theta = 9.85°$, 22.4° and 30.0° (Fig. 1b), and therefore, the presence of these peaks within the P/Z composite proved the existence of zeolite X within the final composite [28]. PANI (Fig. 1a) exhibits a comparatively semi-crystalline nature due to the presence of benzenoid and quinonoid groups within PANI; the patterns show sharp peaks [28]. However, by encapsulation of PANI within the zeolite channels, the alignment and arrangements of PANI chains were improved, and as a result, the intensity of the peaks related to the composite (Fig. 1c) was increased [28, 31].

SEM was used to inspect the surface morphology of PANI, zeolite X and the P/Z composite and estimate the presence and therefore structure of both materials. SEM images of PANI, zeolite X and the P/Z composite are shown in Fig. 3. The zeolite aggregates presented in Fig. 3b contain small crystals denoting short diffusional pathways. These short pathways, in conjunction with the large surface-diffusion coefficients for zeolites, make the inclusion of PANI easier and faster, as indicated by the easy combination of zeolite X and PANI [28]. The SEM image of pure PANI (Fig. 3a) showed a distinct orientation from that of zeolite X. SEM images also demonstrated that the orientation of PANI in the composite structure (Fig. 3c) was decreased in comparison with that of pure PANI due to the increased agglomeration of zeolite. The diameter of the P/Z composite was between 300 and 600 nm, which may be due to the accumulation of single PANI chains released from the zeolite layers (Fig. 3c); it has been reported that one zeolite layer contains many PANI chains [28, 32].

Additionally, TEM images of the PANI rods, zeolite X and P/Z composite are shown in Fig. 3. The bright field TEM image corresponding to zeolite X (Fig. 3e) indicates typical hexagonal morphology, whereas the image of PANI (Fig. 3d) presents fibrous morphology and indicates that the dimensions of the PANI fibres ranged from 150 to 200 nm in width [33]. Zeolite X particles were distributed within the polymer matrix inside the PANI chains, as can be determined from Fig. 4f. The dark spots within the chains in the TEM image represent zeolite X particles and demonstrate the presence of both zeolite X particles and PANI rods within the resulting composite.

Pure PANI, zeolite X and P/Z composites were characterized by TGA to assess their thermal stability. The TGA analysis of zeolite X (Fig. 4b) revealed two weight loss regions. In the first region, a weight loss of 13% occurred in the temperature range of 49–113 °C, which corresponds to the loss of water within the zeolite structure [34]. The second weight loss region was above 200 °C and could be attributed to the complete combustion of organic substances in the zeolite

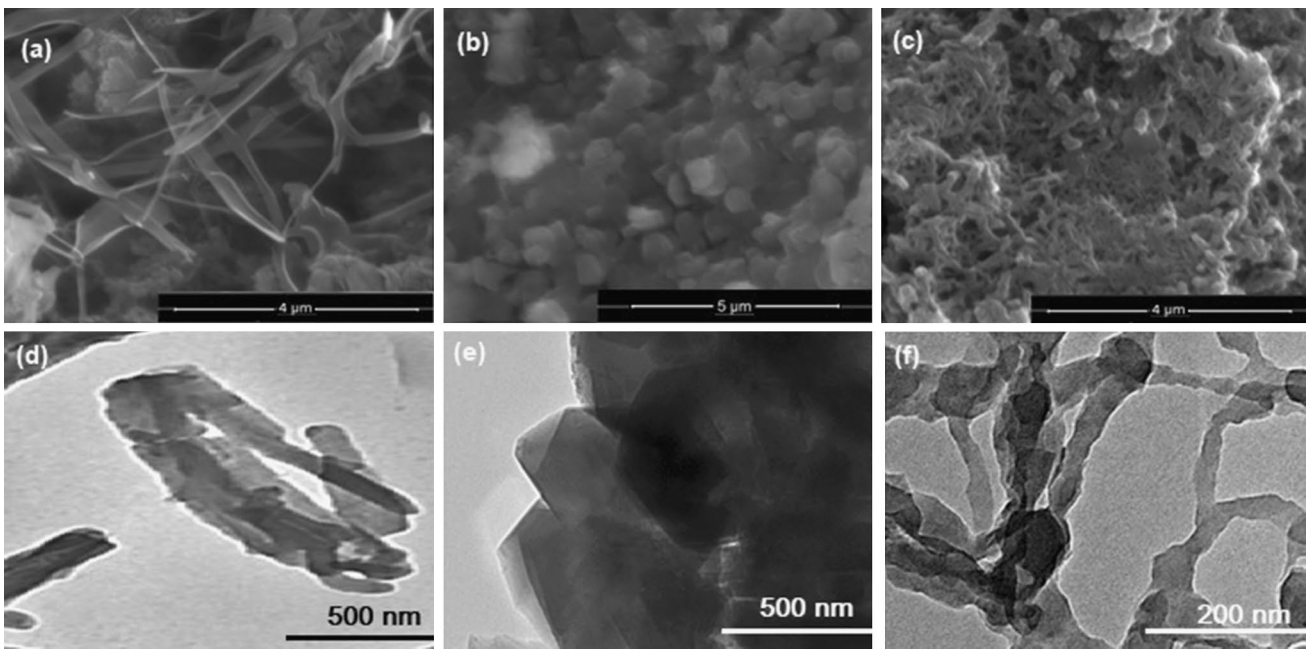


**Fig. 3** SEM image of **a** polyaniline, **b** zeolite X, **c** polyaniline/zeolite X composite and TEM image of **d** polyaniline, **e** zeolite X, **f** polyaniline/zeolite X composite

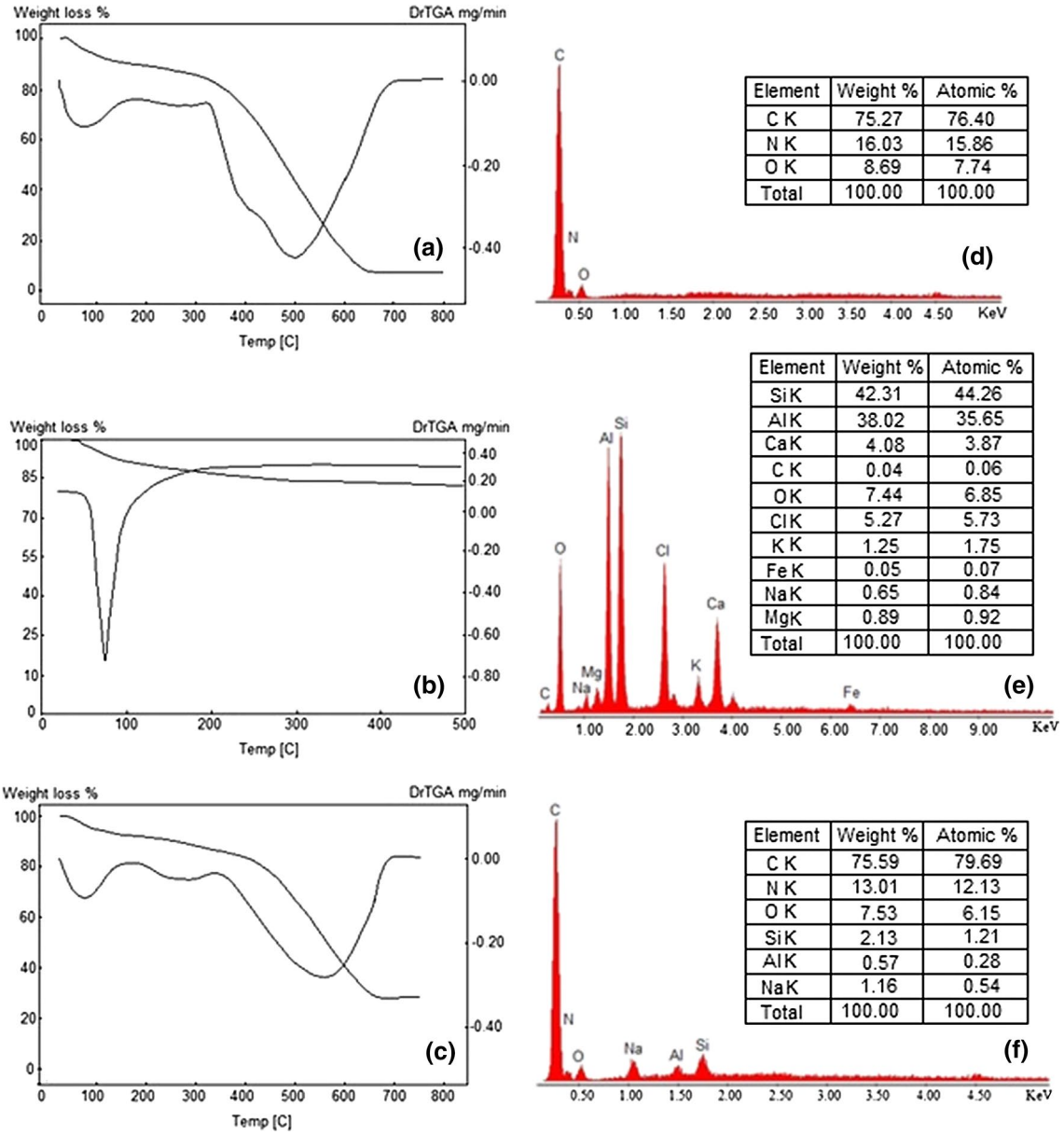


**Fig. 4** TGA thermogram and EDX image of **a**, **d** polyaniline, **b**, **e** zeolite X and **c**, **f** polyaniline/zeolite X composite

X structure, such as the breakdown of the bonds between the silicon and oxygen that make up the zeolite X structure [35, 36]. The PANI TGA thermogram (Fig. 4a) showed two distinct stages of weight loss. An initial weight loss of 25% was observed over the range of 100–250 °C. This result is attributed to the loss of moisture, low molecular weight oligomers, and residual solvent and is consistent with a number of previous reports by other groups. The second weight loss of 60% indicated that PANI began to degrade at 300 °C and was completely decomposed at 630 °C [37]. The TGA analysis of the P/Z composite (Fig. 4c) showed that the weight loss at 30–200 °C corresponds to the removal of water molecules [31]. PANI chains within the composite blocked a part of the active surface of the zeolite X framework for the bonding of water molecules [33]. The augmented thermal stability of PANI in the P/Z composite can be explained by the strong interaction between PANI and zeolite X, which restricts the thermal motion of PANI chains.

To show the elemental distribution of the composite material, EDX spectroscopy was used. The results indicated the incorporation of PANI chains inside the zeolite X structure. For PANI (Fig. 4d), only peaks corresponding to C, O and N were displayed, and a high carbon content was observed [38]. The EDX spectrum for zeolite X (Fig. 4e) showed Al, Si, Na and other peaks, with high Al and Si contents [39]. The presence of bands attributed to aluminium and silicon

within the EDX spectrum of the composite (Fig. 4f) indicated the incorporation of PANI into the zeolite X structure.

## Corrosion studies

### Weight loss measurements

The weight loss of carbon steel, 304 and 316 SS alloys and aluminium metal samples was determined after 72 h of immersion in saline water for bare and coated samples (Fig. 2c, f). The results showed that the CR of the coated samples was less than that of the bare samples.

The slope of each line (weight loss per unit time; mg $cm^{-2}$ $h^{-1}$) corresponded to the CR of the tested samples under the required conditions. The weight loss diminished for the coated samples (i.e. CR was suppressed), and thus, corrosion inhibition was reinforced. By using the calculated CR, the corrosion IE (Eq. 2) of the prepared coating was obtained for the samples. The IE results showed that the prepared P/Z anticorrosion coating had a substantial impact on all tested samples, and the carbon steel inhibition efficiency of 81.19% evidenced the formation of a protective film on the metal surface.

### Potentiodynamic polarization studies

Potentiodynamic polarization curves of the metals were collected at polarizing potentials varying from − 200 mV to + 200 mV (versus SCE) at a scan rate of 0.5 mV/s [40] in saline water. The resulting currents were plotted on a logarithmic scale. The numerical values of the variation in $i_{corr}$, $E_{corr}$, slope ($\beta_a$ and $\beta_c$) and CR for the coated and bare samples are shown in Table 2. The cathodic and anodic curves exhibited Tafel-type behaviour. Cyclic polarization was used to test pitting corrosion in the SS and aluminium samples. The method of cyclic polarization includes scanning the potential until reaching a vertex potential and reversing at the current threshold after crossing the vertex potential. The pitting corrosion of SS and aluminium is manifested by an increase in current upon achieving a specific anode potential, $E_{pitt}$. According to the current understanding of the pitting corrosion process, $E_{pitt}$ represents a critical threshold value where metastable pit nuclei within the passive state of SS may be transformed into stable growing pits when the passive formation breaks down [41].

The polarization corrosion curves of bare and coated SS304 in saline water are shown in Fig. 5a, b, respectively. A summary of the overall results, including $\beta_a$, $\beta_c$, $E_{corr}$, $i_{corr}$ and CR (MPY), is presented in Table 2. In the coated sample, there was a significant increase in $\beta_a$ and $\beta_c$ due to the formation of a protective layer. Changes in $\beta_a$ and $\beta_c$ may correspond to completely different mechanisms in the process of corrosion inhibition. A decrease in $E_{corr}$ from − 266.6 mV (bare sample) to − 335.5 mV (coated sample) is shown in Table 2; $i_{corr}$ decreased from 5.287 to 1.018 µA/$cm^2$, and therefore, CR decreased from 2.403 MPY for the bare electrode to 0.3132 MPY for the coated one. These results showed that the CR of bare steel is greater than that of coated steel in the test solution. These effects could also be due to chloride ion ($Cl^-$) penetration, which causes film breakdown and initiates anodic dissolution of the alloy. From these data, the P/Z composite coating protected the alloy surface from corrosive ion attack.

The corrosion protection of P/Z-coated SS316 (Fig. 5d) in saline water was estimated by Tafel extrapolation plots and compared with that of the bare sample (Fig. 5c). The Tafel parameters including $E_{corr}$, $i_{corr}$, $\beta_a$, $\beta_c$, and therefore, CR (in MPY) were recorded and are given in Table 2. The $E_{corr}$ of bare SS316 was − 283.9 mV, but that of coated SS316 was − 288.0 mV. The $i_{corr}$ of bare steel (2.407 µA/$cm^2$) was greater than that of coated steel (1.205 µA/$cm^2$). These data showed that there was a decrease in the magnitude of $i_{corr}$ and a rise in the Tafel constants. Additionally, $E_{corr}$ for the coated SS316 was less than that of bare SS316. All of these results led to a decrease in CR for the coated SS316; thus, corrosion resistance in this medium was shown by the P/Z coating [42].

The potentiodynamic polarization curves for bare and P/Z-coated Al electrodes in the test solution are shown in Fig. 5e, f, respectively. The $E_{corr}$ of the coated Al

**Table 2** Corrosion potential ($E_{corr}$), corrosion current density ($i_{corr}$) calculated by Tafel extrapolation method

| Substrate | Tafel calculations | | | | |
|---|---|---|---|---|---|
| | $E_{corr}$ (mV) | $i_{corr}$ (µA/$cm^2$) | $\beta_a$ (mV/dec) | $\beta_c$ (mV/dec) | CR (MPY) |
| SS304 bare | − 266.6 | 5.287 | $50.81 * 10^{-3}$ | $174.9 * 10^{-3}$ | 2.403 |
| SS304 coated | − 335.5 | 1.018 | $189.3 * 10^{-3}$ | $283.4 * 10^{-3}$ | 0.3132 |
| SS 316 bare | − 283.9 | 5.407 | $58.93 * 10^{-3}$ | $206.1 * 10^{-3}$ | 1.094 |
| SS 316 coated | − 288.0 | 1.005 | $71.08 * 10^{-3}$ | $318.3 * 10^{-3}$ | 0.2733 |
| Al-bare | − 860.0 | 84.66 | $170.2 * 10^{-3}$ | 1.117 | 23.48 |
| Al-coated | − 820.2 | 32.78 | $14.19 * 10^{-3}$ | $108.5 * 10^{-3}$ | 0.2506 |
| C-steel bare | − 658.1 | 77.22 | $35.22 * 10^{-3}$ | $335.6 * 10^{-3}$ | 35.09 |
| C-steel coated | − 610.9 | 23.79 | $164.1 * 10^{-3}$ | $434.6 * 10^{-3}$ | 10.81 |

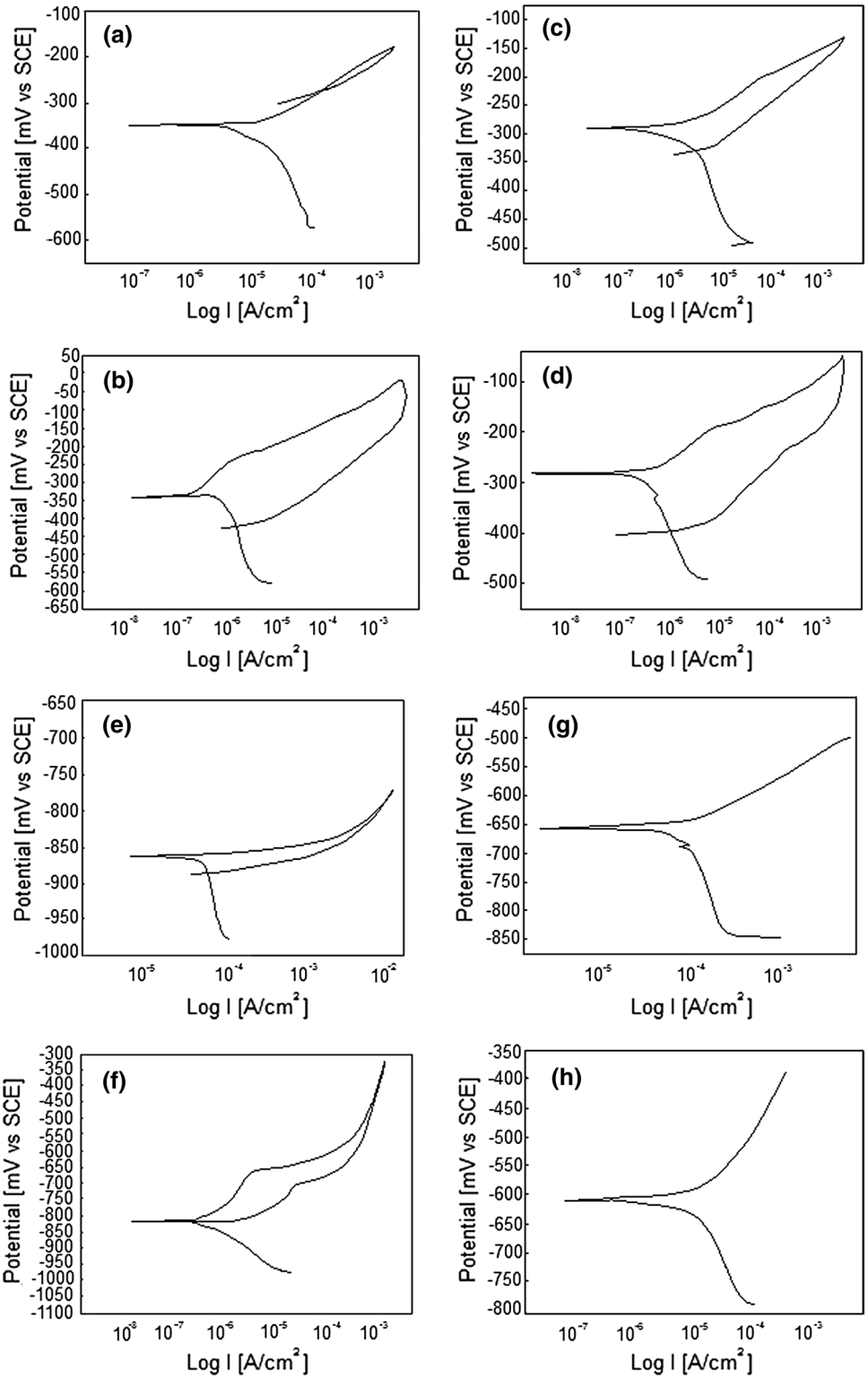


**Fig. 5** Polarization curves of **a**, **b** bare and coated SS304, **c**, **d** bare and coated SS316, **e**, **f** bare and coated Al and **g**, **h** bare and coated carbon steel immersed in saline water

electrodes was shifted in the positive direction compared to that of the bare electrode (Fig. 5f). $E_{corr}$ increased from − 860.0 mV for bare Al to − 820.2 mV versus SCE for the P/Z-coated Al electrode. The positive shift in $E_{corr}$ indicated the protection of the Al surface by the P/Z coating (anodic protection) [43]. Both the cathodic and anodic currents decreased significantly when Al was coated with P/Z. The values of $E_{corr}$, $i_{corr}$, $\beta_a$, $\beta_c$ and CR (in MPY) obtained from these curves are given in Table 2.

The potentiodynamic polarization curves of bare and coated carbon steel immersed in saline water at room temperature (25 ± 3 °C) are shown in Fig. 5g, h, respectively; the corrosion parameters are given in Table 2. Upon immersion of bare carbon steel in the test solution, $E_{corr}$ was recorded at − 658.1 mV versus SCE. For the coated carbon steel, $E_{corr}$ shifted in the positive direction to − 610.9 mV versus SCE. This shift indicated that a film had been formed on the anodic sites of the metal surface [44]. The formation of a protective film on the metal surface is further supported by the fact that $\beta_a$ increased from 35.22 * $10^{-3}$ to 164.1 * $10^{-3}$ mV/dec. Furthermore, $i_{corr}$ diminished from 77.22 to 23.79 µA/cm$^2$. Thus, the polarization study confirmed the formation of a protective film on the metal surface.

### Electrochemical impedance spectroscopy

The negative of imaginary impedance plotted against real impedance (Nyquist plot) and corresponding fitting Nyquist plots for bare and coated SS304 is presented in Fig. 6a–d. The impedance spectrum can be described by a single semicircle in the complex plane. As shown in Fig. 6a, the impedance diagram of bare SS304 is in the shape of a semicircle, and the $R_{ct}$ value representing the charge transfer resistance of the steel/electrolyte interface is equal to the diameter of the semicircle, which was 1.12 Ω cm$^2$; the corresponding diameter for coated SS304 was 55.79 Ω cm$^2$. Bare SS304 exhibited low polarization resistance due to the easy attack of corrosive chloride ions on steel surfaces. The $R_{ct}$ value of coated SS304 represents the charge transfer resistance of the steel/electrolyte interface, and the polymer coating resistance in the test solution was significantly higher than that of the bare steel due to the inhibition of electron transfer to the polymer from the metal (Table 3). The impedance spectra were fitted and analysed by using an equivalent circuit model (Fig. 6i) that has been used and reported elsewhere to describe the steel/electrolyte interface [45, 46]. The impedance data were best fitted by the CPE model because coatings have irregularities, defects and rough surfaces, which permit the solution to penetrate the coating surface. This widely accepted scheme has been deduced to represent the electrochemical behaviour of metals covered with a coated film [47]. CPE was defined by Eq. (3), $\omega$ was defined and calculated by Eq. (4), and $C_{dl}$ for both cases was calculated using Eq. (5). The impedance parameters, including $R_s$, $R_{ct}$, $Y_0$, $n$, $C_{dl}$ and IE (%), were calculated and are given in Table 3. As shown in Table 3, the $C_{dl}$ values tended to decrease for the bare sample and increase for the coated sample, and IE also increased. The decrease in $C_{dl}$ may be attributed to a decrease in the local dielectric constant and/or an increase in the thickness of the electrical double layer.

The typical impedance–frequency Bode plots for bare and coated SS304 samples and therefore the impedance at the lowest studied frequency (0.01 Hz) are shown in Fig. 7a, b. The increase in impedance values for the coated SS is attributed to the growth of the passive film over the surface of the SS electrode and the good behaviour of the tested coating. Additionally, the frequency–phase Bode plots for bare and coated SS (Fig. 7c, d) showed that the maximum phase angle for bare SS304 was 16° and for coated SS304 was 80° and was shifted towards the lower-frequency range (1000–100 Hz for bare) and at higher-frequency range (10,000–1000 Hz for coated SS304). The shifting of the phase angle at the lower frequency was attributed to the formation of double-layer capacitance and the reduction in the anodic surface area of the coating [48]. This phenomenon indicated that the surface was covered with a protective coating layer on the surface. It was apparent from Nyquist plots that the impedance response of SS304 steel changed considerably after being coated.

The corrosion behaviour of bare and P/Z composite-coated SS316 in the tested medium was revealed by EIS methods. The Nyquist (Fig. 6e) and corresponding fitted Nyquist plots (Fig. 6f) of the impedance behaviour of the bare sample and the Nyquist (Fig. 6g) and corresponding fitted Nyquist plots (Fig. 6h) of the coated samples were modelled by the equivalent circuit depicted in Fig. 6i. The impedance parameters, such as ($R_s$), ($R_{ct}$) and ($C_{dl}$), derived from these curves are given in Table 3. $R_{ct}$ is the charge transfer resistance of the area at the metal/coating interface at which corrosion occurs and $C_{dl}$ is the corresponding capacitance. CPE was defined by Eq. (3), and the angular frequency ($\omega$) defined and calculated by Eq. (4) and capacitance ($C$) of the double layer for each case were calculated using Eq. (5). The EIS Nyquist plots consisted of a single capacitance loop, as clearly observed. The impedance of the coated sample was considerably larger than that of the bare sample. The values of IE (%) were calculated using Eq. (6). The $R_{ct}$ increased from 3.39 Ω cm$^2$ for bare SS to 668.33 Ω cm$^2$ for the coated sample, and $C_{dl}$ showed an increased value for the coated sample with 99.49% IE.

The typical impedance–frequency Bode plots for bare and coated samples and therefore the impedance (at a frequency of 0.01 Hz) are shown in Fig. 7e, f, respectively. The impedance values for the coated SS were higher than those for the bare SS due to the growth of the passive film on the surface of the SS electrode and the smart behaviour of the tested coating. The frequency–phase Bode plots for bare and coated SS316 in Fig. 7g, h, respectively, showed that the maximum phase angle for bare SS316 was 13° in the lower-frequency range and that the angle for coated SS316 was 32° at a higher frequency. From the above-mentioned results, the P/Z coating inhibited the corrosion of SS316.

The typical Nyquist plot and corresponding fitting impedance plots of bare and coated Al electrodes are shown in Fig. 6j, k, respectively. The plots were recorded at an

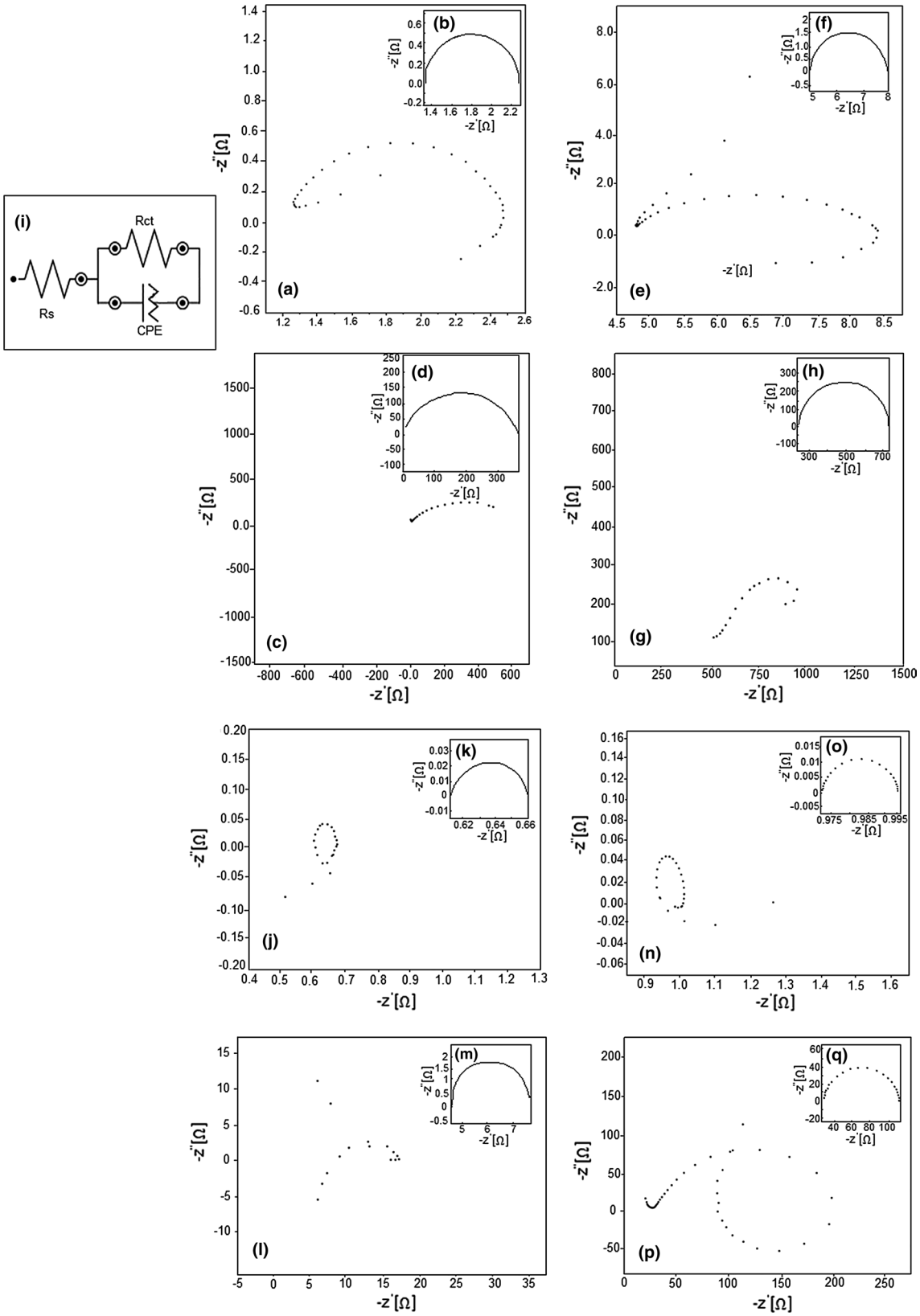


**Fig. 6** Nyquist plots and fitted Nyquist pilots for **a**, **b** bare, **c**, **d** coated SS304; **e**, **f** bare, **g**, **h** coated SS316; **j**, **k** bare, **l**, **m** coated Al; **n**, **o** bare, **p**, **q** coated carbon steel and **i** the electrochemical equivalent circuit used to fit the impedance spectra

**Table 3** Electrochemical impedance parameters for SS304, SS316, carbon steel and aluminium metal in saline water for bare and coated samples

| Samples | $R_s$ (Ω cm$^2$) | $R_{ct}$ (Ω cm$^2$) | $Y_0$ (mF) | $C_{dl}$ (F cm$^{-2}$) | $n$ | $E$ (%) |
|---|---|---|---|---|---|---|
| Bare SS304 | 1.28 | 1.12 | 845.8 | 948.99 | 0.9984 | – |
| Coated SS304 | 61.26 | 55.79 | 229.05 | 12,781.52 | 0.9962 | 97.99 |
| Bare SS316 | 4.76 | 3.39 | 469.49 | 1595.29 | 0.9994 | – |
| Coated SS316 | 369.77 | 668.33 | 15.86 | 10,606.12 | 0.9953 | 99.49 |
| Bare C-steel | 903.37 | 80.64 | 336.16 | 27,112.67 | 1.0001 | – |
| Coated C-steel | 32.31 | 172.52 | 216.51 | 37,356.03 | 0.9990 | 53.26 |
| Bare Al | 607.25 | 65.52 | 353.41 | 23,161.54 | 1.0029 | – |
| Coated Al | 3.44 | 106.92 | 308.11 | 32,947.86 | 0.9956 | 38.72 |

open-circuit potential in an aqueous solution of saline water. These impedance plots were modelled by the equivalent circuit depicted in Fig. 6i. Although there was excellent agreement between the experimental and simulated data generated using the same equivalence circuit, there was also a substantial distinction between the bare and P/Z-coated Al. The values of the parameters fitted to the experimental data using the circuit of Fig. 6i for bare and coated Al are presented in Table 3. From the measured charge transfer resistance values shown in Table 3, the parameter values of coated Al were considerably different from those obtained for bare Al. CPE, $\omega$ and $C$ were defined by Eqs. 3–5, and IE (%) was calculated by Eq. (6). The $R_{ct}$ value of 106.92 Ω cm$^2$ for coated Al represented an increase from the value of 65.52 Ω cm$^2$ for the bare Al sample, corresponding to a 38.72% protection efficiency.

The typical impedance–frequency Bode plots for the bare and coated Al samples are shown in Fig. 8a, b. The impedance at the lowest studied frequency (0.01 Hz) was 0.6 Ω for the bare sample and 7.6 Ω for the coated Al, indicating an increase for the coated Al in the solution. This increased impedance demonstrated the formation of a protective passive oxide film on the coating surface. Additionally, the frequency–phase Bode plots for the bare and coated Al are shown in Fig. 8c, d, respectively, and show that the maximum phase angle was 2° for bare Al and 17° for coated Al. This result revealed the anticorrosion properties of the prepared P/Z coating with respect to Al.

The corrosion inhibition behaviour of carbon steel after immersion in the test solution was investigated by EIS. The impedance Nyquist diagram and the fitted Nyquist diagram for bare and coated carbon steel are shown in Fig. 6n, o, respectively. The equivalent circuit model for this technique is shown in Fig. 6i. The values of $R_s$ and $R_{ct}$ were obtained from the Nyquist plots. CPE, $\omega$ and $C$ were defined by Eqs. 3–5, and IE (%) was calculated by Eq. (6). The impedance parameters for the corrosion of carbon steel are given in Table 3. For the coated sample, $R_{ct}$ and IE (%) were increased: the $R_{ct}$ value for bare carbon steel was 80.64 Ω cm$^2$, and the value for the coated sample was 172.52 Ω cm$^2$. The complex impedance plots show one capacitive contribution represented by one semicircle for the coated sample, which may be due to the resistance and capacitance of the coating [49, 50]. Measured impedance loops are often depressed semicircles with their centre below the real axis. The increase in impedance was attributed to the growth of passive film thickness and the increase in film resistance itself towards the penetration of aggressive ions through the film [51]. The increase in impedance was more significant for the coated sample than for the bare sample.

The frequency Bode plots for bare and coated steel are shown in Fig. 8e, f, respectively, whereas the frequency–phase Bode plots are shown in Fig. 8g, h for bare and coated samples, respectively. The frequency–phase Bode plots showed that the maximum phase angle was at 35° for coated steel, which was higher than that for the bare sample (0.6°). From these results, the P/Z coating acts as a real barrier against the penetration of ions from solution.

## Conclusion

From this study, the following conclusions were drawn. The P/Z composite coating was successfully prepared by the traditional oxidation polymerization method; the integration of the polyaniline within the zeolite channels was confirmed by FTIR, UV–visible, TGA, SEM, TEM, EDX and XRD investigations which proved the successful synthesis of the composite coating. SEM and TEM images confirmed the presence of polyaniline chains inside zeolite X channels. Corrosion and electrochemical techniques were used to evaluate the coating protection of the studied metals and alloys. Weight loss technique, potentiostatic polarization (Tafel polarization) and EIS spectroscopy techniques showed an adequate effect of the P/Z coating in corrosion mitigation on the surface of various materials including SS (304 and 316 grades), aluminium and carbon steel samples in saline water.

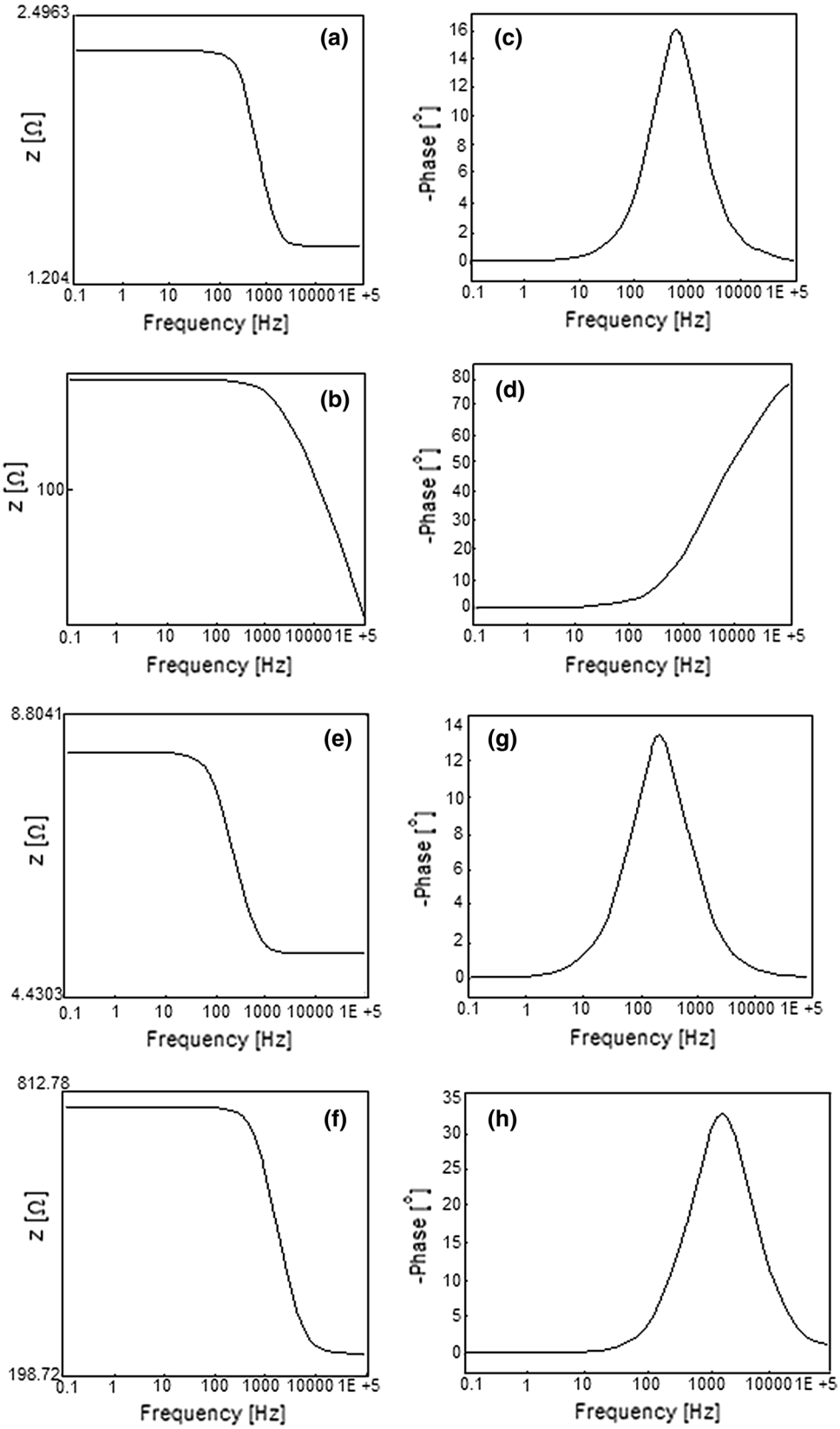


**Fig. 7** Frequency Bode modules (**a**, **b**) for bare and coated SS304; frequency–phase Bode plots (**c**, **d**) for bare and coated SS304; frequency Bode modules (**e**, **f**) for bare and coated SS316 and frequency–phase Bode plots (**g**, **h**) for bare and coated SS316

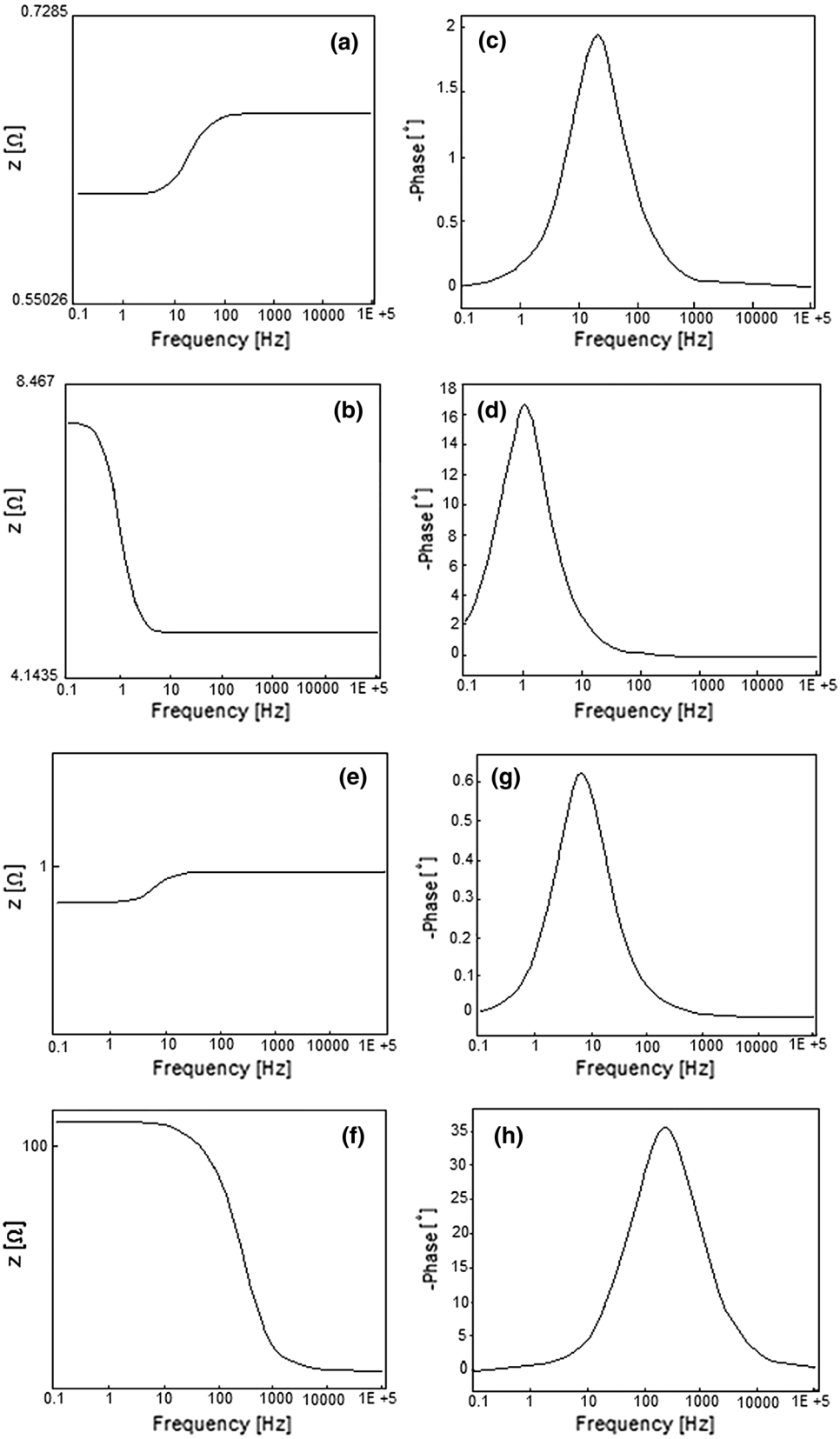


**Fig. 8** Frequency Bode modules (**a**, **b**) for bare and coated Al; frequency–phase Bode plots (**c**, **d**) for bare and coated Al; frequency Bode modules (**e**, **f**) for bare and coated carbon steel and frequency–phase Bode plots (**g**, **h**) for bare and coated carbon steel

## Compliance with ethical standards

**Conflict of interest** The authors declare that they have no conflict of interest.



## References

1. Shatat M, Riffat SB (2012) Water desalination technologies utilizing conventional and renewable energy sources. Int J Low-Carbon Technol 9:1–19. https://doi.org/10.1093/ijlct/cts025
2. Al-Zahrani A, Orfi J, Al-Suhaibani Z, Salim B, Al-Ansary H (2012) Thermodynamic analysis of a reverse osmosis desalination unit with energy recovery system. Procedia Eng 33:404–414. https://doi.org/10.1016/j.proeng.2012.01.1220
3. Greenleea LF, Lawlerb DF, Freemana BD, Marrotc B, Moulinc P (2009) Reverse osmosis desalination: water sources, technology and today's challenges. Water Res 43:2317–2348. https://doi.org/10.1016/j.watres.2009.03.010
4. Cheng W, Feng J, Fuhui W (2004) The characterization and corrosion resistance of cerium chemical conversion coatings for 304 stainless steel. Corros Sci 46:75–89. https://doi.org/10.1016/S0010-938X(03)00135-5
5. Ram MK, Yavuz O, Lahsangah V, Aldissi M (2005) CO gas sensing from ultrathin nano-composite conducting polymer film. Sens Actuat B Chem 106:750–757. https://doi.org/10.1016/j.snb.2004.09.027
6. Chen XJ, Luo C, Zhang ZH, Zhao M (2012) Preparation and anticorrosion properties of polyaniline-containing coating on Mg–Li alloy. Anti-Corrosion Methods Mater 59:291–298. https://doi.org/10.1108/00035591211274406
7. Ansari R (2006) Application of polyaniline and its composites for adsorption/recovery of chromium(VI) from aqueous solutions. Acta Chim Slov 53:88–94
8. Zarras P, Anderson N, Webber C, Irvin DJ, Irvin JA, Guenthner A, Stenger-Smith JD (2003) Progress in using conductive polymers as corrosion-inhibiting coatings. Radiat Phys Chem 68:387–394. https://doi.org/10.1016/S0969-806X(03)00189-0
9. Spinks GM, Dominis AJ, Wallace GG, Tallman DE (2002) Electroactive conducting polymers for corrosion control. J Solid State Electrochem 6:85–100. https://doi.org/10.1007/s100080100
10. Bernard MC, Joiret S, Goff AHL, Phong PV (2001) Protection of iron against corrosion using a polyaniline layer: III. Spectroscopic analysis of the mechanisms accompanying the breakdown. J Electrochem Soc 148:B304–B306. https://doi.org/10.1149/1.1380672
11. Silva JEP, Torresi SIC, Torresi RM (2007) Polyaniline/poly (methyl methacrylate) blends for corrosion protection: the effect of passivating dopants on different metals. Prog Org Coat 58:33–39. https://doi.org/10.1016/j.porgcoat.2006.11.005
12. Vitoratos E, Sakkopouos S, Dalas E, Malkaj P, Anestis Ch (2007) D.C. conductivity and thermal aging of conducting zeolite/polyaniline and zeolite/polypyrrole blends. Curr Appl Phys 7:578–581. https://doi.org/10.1016/j.cap.2006.12.001
13. Banerjee PC, Woo RP, Grayson SM, Majumder A, Raman RKS (2014) Influence of zeolite coating on the corrosion resistance of AZ91D magnesium alloy. Materials 7:6092–6104. https://doi.org/10.3390/ma7086092
14. Sirivat A, Chotpattananont D, Hiamtup P, Schwank J (2005) Electrical conductivity of polyaniline/zeolite composites and synergetic interaction with CO. Mater Sci Eng B 117:276–282. https://doi.org/10.1016/j.mseb.2004.12.006
15. Ashassi-Sorkhabi H, Seifzadeh D, Hosseini MG (2008) EN, EIS and polarization studies to evaluate the inhibition effect of 3H-phenothiazin-3-one, 7-dimethylamin on mild steel corrosion in 1 M HCl solution. Corros Sci 50:3363–3370. https://doi.org/10.1016/j.corsci.2008.09.022
16. Roeper DF, Chidambaram D, Clayton CR, Halada GP (2008) Development of an environmentally friendly protective coating for the depleted uranium–0.75 wt% titanium alloy: Part V. Electrochemical impedance spectroscopy of the coating. Electrochim Acta 53:2130–2134. https://doi.org/10.1016/j.electacta.2007.09.021
17. Kim CH, Pyun SI, Kim JH (2003) An investigation of the capacitance dispersion on the fractal carbon electrode with edge and basal orientations. Electrochim Acta 48:3455–3463. https://doi.org/10.1016/S0013-4686(03)00464-X
18. Jorcin JB, Orazem ME, Pebere N, Tribollet B (2006) CPE analysis by local electrochemical impedance spectroscopy. Electrochim Acta 51:1473–1479. https://doi.org/10.1016/j.electacta.2005.02.128
19. Mahdavian M, Attar MM (2009) Electrochemical behaviour of some transition metal acetylacetonate complexes as corrosion inhibitors for mild steel. Corros Sci 51:409–414. https://doi.org/10.1016/j.corsci.2008.11.010
20. Ibrahim KA (2017) Synthesis and characterization of polyaniline and poly (aniline-co-o-nitro aniline) using vibrational spectroscopy. Arab J Chem 10:S2668–S2674. https://doi.org/10.1016/j.arabjc.2013.10.010
21. Butoi B, Groza A, Dinca P, Balan A, Barna V (2017) Morphological and structural analysis of polyaniline and poly(*o*-anisidine) layers generated in a DC glow discharge plasma by using an oblique angle electrode deposition configuration. Polymers 9:1–18. https://doi.org/10.3390/polym9120732
22. Khan R, Khare P, Baruah BP, Hazarika AK, Dey NC (2011) Spectroscopic, kinetic studies of polyaniline-flyash composite. Adv Chem Eng Sci 1:37–44. https://doi.org/10.4236/aces.2011.12007
23. Tang SJ, Lin KY, Zhu YR, Huang HY, Ji WF, Yang CC, Chao YC, Yeh JM, Chiu KC (2013) Structural and electrical characterization of polyanilines synthesized from chemical oxidative polymerization via doping/de-doping/re-doping processes. J Phys D Appl Phys 46:505301. https://doi.org/10.1088/0022-3727/46/50/505301
24. Tang SJ, Wang AT, Lin SY, Huang KY, Yang CC, Yeh JM, Chiu KC (2011) Polymerization of aniline under various concentrations of APS and HCl. Polym J 43:667–675. https://doi.org/10.1038/pj.2011.43
25. Baran R, Millot Y, Onfroy T, Krafft JM, Dzwigaj S (2012) Influence of the nitric acid treatment on Al removal, framework composition and acidity of BEA zeolite investigated by XRD, FTIR and NMR. Microporous Mesoporous Mater 163:122–130. https://doi.org/10.1016/j.micromeso.2012.06.055
26. Ojha K, Pradhan NC, Samanta AN (2004) Zeolite from fly ash: synthesis and characterization. Bull Mater Sci 27:555–564. https://doi.org/10.1007/BF02707285
27. Olad A, Naseri B (2010) Preparation, characterization and anticorrosive properties of a novel polyaniline/clinoptilolite nanocomposite. Prog Org Coat 67:233–238. https://doi.org/10.1016/j.porgcoat.2009.12.003
28. Jamil TS, Shaban AM, Shalaby MS, Souaya ER, Sedra MR, Abd El Aziz AH (2018) Synthesis and characterization of polyaniline/zeolite X composites as anticorrosion coating materials. Polym

Sci Ser B 60:387–394. https://doi.org/10.1134/S1560090418030120
29. Ozdemir C, Can HK, Kolac N, Guner A (2006) Synthesis, characterization, and comparison of self-doped, doped, and undoped forms of polyaniline, poly(o-anisidine) and poly[aniline-*co*-(o-anisidine)]. J Appl Polym Sci 99:2182–2192. https://doi.org/10.1002/app.22718
30. Changa KC, Jang GW, Peng CW, Lin CY, Shieh JC, Yeh JM, Yang JC, Li WT (2007) Comparatively electrochemical studies at different operational temperatures for the effect of nanoclay platelets on the anticorrosion efficiency of DBSA-doped polyaniline/$Na^+$–MMT clay nanocomposite coatings. Electrochim Acta 52:5191–5200. https://doi.org/10.1016/j.electacta.2007.01.088
31. Shyaa AA, Hasan OA, Abbas AM (2015) Synthesis and characterization of polyaniline/zeolite nanocomposite for the removal of chromium (VI) from aqueous solution. J Saudi Chem Soc 19:101–107. https://doi.org/10.1016/j.jscs.2012.01.001
32. Frisch HL, Song H, Ma J, Rafailovich M, Zhu S, Yang NL, Yan X (2001) Antiferromagnetic pairing in polyaniline salt-zeolite nanocomposites. J Phys Chem B 105:11901–11905. https://doi.org/10.1021/jp012278z
33. Marjanović GC, Dondur V, Milojević M, Mojović M, Mentus S, Radulović A, Vuković Z, Stejskal J (2009) Synthesis and characterization of conducting self-assembled polyaniline nanotubes/zeolite nanocomposite. Langmuir 25:3122–3131. https://doi.org/10.1021/la8030396
34. Mansouri N, Rikhtegar N, Panahi HA, Atabi F, Shahraki BK (2013) Porosity, characterization and structural properties of natural zeolite—clinoptilolite—as a sorbent. Environ Prot Eng 39:139–152. https://doi.org/10.5277/EPE130111
35. Giroux M, Sahadeo E, Libera R, Maurizi A, Giles I, Marteel-Parrish A (2016) An undergraduate research experience: synthesis, modification, and comparison of hydrophobicity of zeolites A and X. Polyhedron 114:42–52. https://doi.org/10.1016/j.poly.2015.09.037
36. Tiseanu C, Gagea B, Parvulescu VI, Lorenz-Fonfria V, Gessner A, Kumke MU (2007) Investigation of the hydrophobization efficiency of terbium-exchanged BEA zeolites by means of FT-IR, TGA, physical adsorption, and time-resolved photoluminescence. Langmuir 23:6781–6787. https://doi.org/10.1021/la063308y
37. Wang SX, Sun LX, Tan ZC, Xu F, Li YS (2007) Synthesis, characterization and thermal analysis of polyaniline (PANI)/$Co_3O_4$ composites. Thermal Anal Calorim 89:609–612. https://doi.org/10.1007/s10973-006-7569-3
38. Rafiqi FA, Majid K (2016) Synthesis, characterization, luminescence and magnetic properties of composite of polyaniline with nickel bisacetylacetonate complex. Polym Sci Ser B 58:371–383. https://doi.org/10.1134/S156009041603012X
39. Jahangirian H, Ismail MHS, Haron MJ, Rafiee-Moghaddam R, Shameli K, Hosseini S, Kalantari K, Khandanlou R, Gharibshahi E, Soltaninejad S (2013) Synthesis and characterization of zeolite/Fe3O4 nanocomposite by green quick precipitation method. Dig J Nanomater Biostruct 8:1405–1413
40. Abdel Ghanyl NA, El-Shenawy AE, Hussien WAM (2011) The Inhibitive effect of some amino acids on the corrosion behaviour of 316L stainless steel in sulfuric acid solution. Mod Appl Sci 5:19–29. https://doi.org/10.5539/mas.v5n4p19
41. Loto RT (2013) Pitting corrosion evaluation of austenitic stainless steel type 304 in acid chloride media. J Mater Environ Sci 4:448–459
42. Shaker RA, Abdulrazak SA, Alsammarraie AMA (2014) Enhancing of corrosion protection properties using electropolymerized polyaniline coating. Arch Appl Sci Res 6:243–255
43. Shabani-Nooshabadi M, Ghoreishi SM, Behpour M (2009) Electropolymerized polyaniline coatings on aluminum alloy 3004 and their corrosion protection performance. Electrochim Acta 54:6989–6995. https://doi.org/10.1016/j.electacta.2009.07.017
44. Raja AS, Rajendran S, Satyabama P (2013) Inhibition of corrosion of carbon steel in well water by DL-phenylalanine–$Zn^{2+}$ system. J Chem 2013:1–8. https://doi.org/10.1155/2013/720965
45. Martinez S, Metikos-Hukovic M (2003) A nonlinear kinetic model introduced for the corrosion inhibitive properties of some organic inhibitors. J Appl Electrochem 33:1137–1142. https://doi.org/10.1023/B:JACH.0000003851.82985.5e
46. Quraishib MA, Singh A, Singh VK, Yadav DK, Singh AK (2010) Green approach to corrosion inhibition of mild steel in hydrochloric acid and sulphuric acid solutions by the extract of Murraya koenigii leaves. Mater Chem Phys 122:114–122. https://doi.org/10.1016/j.matchemphys.2010.02.066
47. Esfahani MN, Pourriahi M, Motalebi A, Zendehdel M (2013) Improvement of the corrosion performance of 304L stainless steel by a nanostructure hybrid coating/henna extract. Anti-Corrosion Methods Mater 61:1–9. https://doi.org/10.1108/ACMM-12-2012-1229
48. Fusco M (2016) Multilayer protective coatings for high-level nuclear waste storage containers. Dissertation, Faculty of North Carolina State University, Raleigh, North Carolina
49. Onofre-Bustamante E, Dominguez-Crespo MA, Torres-Huerta AM, Olvera-Martinez A, Genesca-Longueras J, Rodriguez-Gomez FJ (2009) Characterization of cerium-based conversion coatings for corrosion protection of AISI-1010 commercial carbon steel. J Solid State Electrochem 13:1785–1799. https://doi.org/10.1007/s10008-009-0871-9
50. Behpour M, Ghoreishi SM, Soltani N, Salavati-Niasari M, Hamadanian M, Gandomi A (2008) Electrochemical and theoretical investigation on the corrosion inhibition of mild steel by thiosalicylaldehyde derivatives in hydrochloric acid solution. Corros Sci 50:2172–2181. https://doi.org/10.1016/j.corsci.2008.06.020
51. Sathiyanarayanan S, Muthukrishnan S, Venkatachari G, Trivedi DC (2005) Corrosion protection of steel by polyaniline (PANI) pigmented paint coating. Prog Org Coat 53:297–301. https://doi.org/10.1016/j.porgcoat.2005.03.007